

On the need for a nonlinear subscale turbulence term in POD models as exemplified for a high-Reynolds-number flow over an Ahmed body

Jan Östh^{1,†}, Bernd R. Noack², Siniša Krajnović¹, Diogo Barros^{2,3} and Jacques Borée²

¹Division of Fluid Dynamics, Department of Applied Mechanics, Chalmers University of Technology, SE-412 96 Göteborg, Sweden

²Institut PPRIME, CNRS – Université de Poitiers – ENSMA, UPR 3346, Département Fluides, Thermique, Combustion, CEAT, 43 rue de l'Aérodrome, F-86036 Poitiers CEDEX, France

³PSA Peugeot Citroën, Centre Technique de Velizy, 78943 Vélizy-Villacoublay CEDEX, France

(Received 22 October 2013; revised 18 February 2014; accepted 22 March 2014)

We investigate a hierarchy of eddy-viscosity terms in proper orthogonal decomposition (POD) Galerkin models to account for a large fraction of unresolved fluctuation energy. These Galerkin methods are applied to large eddy simulation (LES) data for a flow around a vehicle-like bluff body called an Ahmed body. This flow has three challenges for any reduced-order model: a high Reynolds number, coherent structures with broadband frequency dynamics, and meta-stable asymmetric base flow states. The Galerkin models are found to be most accurate with modal eddy viscosities as proposed by Rempfer & Fasel (*J. Fluid Mech.*, vol. 260, 1994*a*, pp. 351–375; *J. Fluid Mech.* vol. 275, 1994*b*, pp. 257–283). Robustness of the model solution with respect to initial conditions, eddy-viscosity values and model order is achieved only for state-dependent eddy viscosities as proposed by Noack, Morzyński & Tadmor (*Reduced-Order Modelling for Flow Control*, CISM Courses and Lectures, vol. 528, 2011). Only the POD system with state-dependent modal eddy viscosities can address all challenges of the flow characteristics. All parameters are analytically derived from the Navier–Stokes-based balance equations with the available data. We arrive at simple general guidelines for robust and accurate POD models which can be expected to hold for a large class of turbulent flows.

Key words: low-dimensional models, turbulence simulation, wakes

1. Introduction

In this work, we address important enablers for low-dimensional proper orthogonal decomposition (POD) models for complex high-Reynolds-number flows. Reduced order models (ROMs) are widely used in fluid mechanics. The purposes range from understanding of the physical mechanisms, to computational inexpensive surrogate models for optimization, to low-dimensional plants for control design. In this study,

† Email address for correspondence: ojan@chalmers.se

we focus on reduced-order Galerkin models, as they have a convenient mathematical structure for the above-mentioned purposes. The Galerkin expansions may arise from mathematical completeness considerations (Busse 1991; Noack & Eckelmann 1994), from eigenfunctions of Navier–Stokes related equations (Joseph 1976; Boberg & Brosa 1988) or empirical data (Holmes *et al.* 2012). The majority of low-dimensional Galerkin models in engineering applications are of an empirical nature and utilize one or another variant of POD. The first dynamical POD model was presented in the pioneering work of Aubry *et al.* (1988). Their ROM describes the coherent structures in the turbulent boundary layer, particularly sweeps or ejections. Other examples are the vortex shedding flow behind a circular cylinder at low Reynolds number (Deane *et al.* 1991; Noack *et al.* 2003), transitional and turbulent boundary layers (Aubry *et al.* 1988; Rempfer & Fasel 1994*b*), a turbulent jet and the mixing layer (Rajae, Karlsson & Sirovich 1994; Ukeiley *et al.* 2001) and lid-driven cavity flow (Cazemier, Verstappen & Veldman 1998).

POD models have been presented for myriad flow configurations, ranging from laminar, to transitional and turbulent states. However, the construction of POD models for broadband turbulence still constitutes a challenge. A rich set of subscale turbulence representations in POD models have been proposed. Aubry *et al.* (1988) and Podvin (2009) employ a single eddy-viscosity term, thus effectively modelling a Navier–Stokes equation (NSE) at lower Reynolds number. Rempfer & Fasel (1994*a,b*) have proposed mode-dependent refinement of eddy viscosities, inspired by spectral eddy viscosities of homogeneous isotropic turbulence. All these subscale turbulence representations constitute linear terms in the mode coefficients. Galletti *et al.* (2004) add an additional linear term to the Galerkin system, calibrating the parameters with a solution matching technique. Several authors have also proposed nonlinear terms. Noack, Morzyński & Tadmor (2011) derive a nonlinear eddy-viscosity model, based on a finite-time thermodynamics (FTT) closure (Noack *et al.* 2008). Nonlinear models based on the Galerkin projection of filtered NSE have been pursued by Wang *et al.* (2011, 2012). An approach of a completely different nature is suggested by Balajewicz, Dowell & Noack (2013). Here, no auxiliary subscale turbulence terms have been introduced in the Galerkin system, but the dissipative effects are incorporated in a generalized POD.

In the present work, we present for the first time a ROM for the highly turbulent flow around a three-dimensional vehicle bluff body, the so-called Ahmed body. The Ahmed model is used in vehicle aerodynamics as a generic test case that reproduces the important flow structures around passenger vehicles (Ahmed, Ramm & Faltin 1984; Duell & George 1999; Spohn & Gillieron 2002; Lienhart & Becker 2003). Recently, the model has been subjected to intensive research for the pursuit of flow control methods capable of reducing the aerodynamic drag on the model, both passive control (Beaudoin & Aider 2008; Krajnović 2013) and active control (Brunn *et al.* 2008; Pastoor *et al.* 2008; Aider, Beaudoin & Wesfreid 2010; Krajnović & Fernandes 2011). In the present study, we focus on the square-back variant of the Ahmed body, which is essentially a bluff body with curved front edges placed in proximity to the ground. This flow poses a severe challenge for the ROM, due to the bi-modal states of the wake that were discovered in the recent study by Grandemange, Gohlke & Cadot (2013), i.e. the flow switches from one semi-stable asymmetric state to another over time scales, T_S , which is of the order of $T_S \approx 100H/U_\infty$, where H is the height of the body and U_∞ is the velocity of the oncoming flow.

In the proposed POD models, we employ the modal eddy-viscosity refinement by Rempfer & Fasel (1994*b*) and the nonlinear eddy-viscosity scaling based on the

FTT framework proposed by Noack *et al.* (2011) to stabilize the long-term solution behaviour. The POD model utilizes a dataset of time-resolved flow fields of the flow around the bluff body. The dataset has been produced by numerical simulations employing the large eddy simulation (LES) technique. The LES data capture the semi-stable asymmetric states and departures from these states. The flow around a similar bluff body was simulated with a LES by Krajnović & Davidson (2003) over one decade ago. The standard Smagorinsky (1963) subgrid stress model was used both in that study and is used in the present study. Although there have been many more intricate subgrid-stress models developed since the days of Smagorinsky half a century ago, his nonlinear model has proved to be robust, highly applicable and very capable of producing unsteady solutions to complex bluff-body flow cases with high accuracy that are able to yield further physical understanding of the flow dynamics. For instance, the same LES technique was used to simulate the flow around an Ahmed body with a 25° angle of the rear slanted surface by Krajnović & Davidson (2005*a,b*), the flow around high-speed trains at low Reynolds numbers by Hemida & Krajnović (2008, 2010), the flow around freight trains by Hemida, Gil & Baker (2010) and Östh & Krajnović (2014), and the flow around a finite tall circular cylinder by Krajnović (2011).

This paper is organized as follows. First, the flow configuration with a car model and the LES that was used to produce the dataset of time-resolved flow are presented (§ 2). Next, the employed Galerkin models with a hierarchy of subscale turbulence representations are outlined (§ 3). Then, the performance of these POD Galerkin models is studied (§ 4) and conclusions and future directions are provided (§ 5).

2. Configuration

This section presents the LES that produced the dataset of flow snapshots serving as input to the empirical Galerkin models. It begins with the description of the geometry of the vehicle model (§ 2.1), followed by the set-up and a brief outline of the LES technique and numerical details of the simulation (§ 2.2). The main features of the flow are lastly presented (§ 2.4).

2.1. The Ahmed body model

The employed LES reproduces a companion experiment at Institute PPRIME (Östh *et al.* 2013). A description of these experiments and a comparison of the LES and particle image velocimetry (PIV) data are included in appendix A. The vehicle model has a square-back geometry. The model length, L , is 0.893 m, the width, W , is 0.35 m and the height of the body, H , is 0.297 m. All four front edges are rounded with a radius of $r = 0.285H$. The model is placed on four cylindrical supports with an oval-shaped cross-section and the ground clearance, h , is $0.168H$ (0.05 m). Similar square-back models with curved fronts were used in the numerical investigation using LES reported in Krajnović & Davidson (2003) and in the joint experimental and numerical study by Verzicco *et al.* (2002). In the present study the Reynolds number based on the height of the model, the free-stream velocity, U_∞ , and the kinematic viscosity of air at room temperature, ν , is $Re_H = 3 \times 10^5$.

2.2. Flow configuration

We consider an incompressible flow of the Ahmed body in a steady finite domain, $\Omega \in R^3$. The flow is described in a Cartesian coordinate system $\mathbf{x} = (x, y, z)$ with

unit vectors \mathbf{e}_x , \mathbf{e}_y , \mathbf{e}_z , respectively. The unit vectors are oriented such that the x -direction corresponds to the streamwise direction. The y -direction corresponds to the wall-normal direction in which the lift force is acting on the bluff body and the z -direction is aligned with the axis of action of the side force on the body. The origin is located at the midpoint of the base face of the Ahmed body. The plane $z = 0$ thus corresponds to the only symmetry plane of the configuration. The time is represented by t . The velocity vector $\mathbf{u} = (u, v, w)$, has u , v and w as its x -, y - and z -components, respectively. The pressure field is denoted by p . In the following, all quantities are normalized with respect to the oncoming velocity U_∞ , the Ahmed body height H and the constant density ρ of the fluid. The flow is described by the incompressible NSE with corresponding initial and boundary conditions, \mathbf{u}_{IC} and \mathbf{u}_{BC} , respectively:

$$\partial_t \mathbf{u} + \mathbf{u} \cdot \nabla \mathbf{u} + \nabla p - \nu \nabla^2 \mathbf{u} = 0, \quad (2.1a)$$

$$\nabla \cdot \mathbf{u} = 0, \quad (2.1b)$$

$$\mathbf{u}(\mathbf{x}, 0) = \mathbf{u}_{IC}(\mathbf{x}) \quad \forall \mathbf{x} \in \Omega, \quad (2.1c)$$

$$\mathbf{u}(\mathbf{x}, t) = \mathbf{u}_{BC}(\mathbf{x}) \quad \forall \mathbf{x} \in \partial\Omega, t \in [0, T]. \quad (2.1d)$$

Here, $\nu = 1/Re_H$ represents the non-dimensionalized kinematic viscosity, or, equivalently, the reciprocal Reynolds number. The length of the investigated time interval $[0, T]$ is $T = 500$ time units, after the flow has converged to its post-transient time. For later reference, we define the residual of the momentum equation,

$$\mathbf{R}(\mathbf{u}) = \partial_t \mathbf{u} + \mathbf{u} \cdot \nabla \mathbf{u} + \nabla p - \nu \nabla^2 \mathbf{u}. \quad (2.2)$$

This residual is considered as function of the velocity field, since the pressure can be computed from the velocity field by the pressure Poisson equation.

2.3. Large eddy simulation (LES)

The database of the time-resolved flow around the Ahmed model that serves as the input to the empirical ROMs was produced using numerical simulations employing the LES technique. The governing filtered incompressible NSEs are closed using the nonlinear subgrid-stress model originally proposed by Smagorinsky (1963). The method has already been used in numerous scientific investigations of vehicle aerodynamics bluff-body flows (see e.g. Krajnović 2002; Hemida 2008; Krajnović 2009; Wassen & Thiele 2009; Östh & Krajnović 2012). The LES equations are discretized by means of a commercial finite-volume code (AVL Fire 2013) using a co-located grid arrangement and the discretized equations are solved for the velocities. The pressure is obtained by a pressure-correction procedure. The employed computational grid consists of 34 million grid points and the obtained spatial resolution was fine enough to be considered a well-resolved LES according to the common conventions in the field (Davidson 2010). The spatial resolution is detailed in appendix B. The convective fluxes are approximated by a blend of 95 % linear interpolation of second-order accuracy (Central Differencing Scheme) and of 5 % upwind differences of first-order accuracy (Upwind Scheme). The diffusive terms containing viscous plus subgrid terms are approximated by a central differencing interpolation of second-order accuracy. The time-marching procedure is done using the implicit second-order accurate three-time level scheme. The computational domain is shown in figure 1. On the inlet a uniform velocity profile in the streamwise

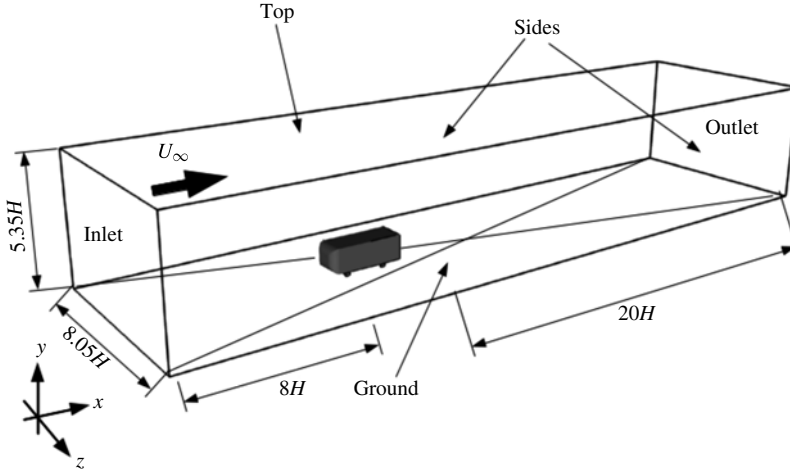


FIGURE 1. The computational domain used in the LES.

direction (x direction) is applied with the free-stream velocity U_∞ . On the outlet the homogeneous Neumann condition is used and on the sides the symmetry condition is used. On the ground a slip condition is set on the first part from the inlet to the body in order to prevent the boundary layer development here. On the rest of the ground the no-slip condition is enforced. This no-slip condition on the ground is set in order to match the experimental set-up, where the model is mounted on a plate above the ground (see appendix A).

2.4. Flow characteristics

Figure 2(a) presents the time history of the normalized drag force signal, C_D , from the simulation. A spectral analysis of the signal reveals several low-frequency peaks at Strouhal numbers $St = fH/U_\infty = 0.036, 0.054, 0.085, 0.12, 0.17$ and 0.21 , but no dominant peak is found, indicating a broadband spectrum of the flow structures in the wake. Figure 2(b) shows the side force signal, C_S . The aerodynamic coefficients are defined as

$$C_D = \frac{F_x}{\frac{1}{2}\rho U_\infty^2 A_x}; \quad C_S = \frac{F_z}{\frac{1}{2}\rho U_\infty^2 A_x}. \quad (2.3a,b)$$

Here, F_x and F_z are the total force (pressure and viscous) integrated over the body in the streamwise and transverse direction, respectively, and $A_x = HW$ is the cross-sectional area of the Ahmed body.

The switch between one bi-modal state to the other is clearly indicated in figure 2(b). The time interval used to plot the forces in figure 2 corresponds to the time-domain that is covered by the snapshots used for the POD and the Galerkin models.

Figure 3 shows a small selection of the flow results in the wake in the plane $y=0$ (indicated in figure 3(e)) to help give an appreciation of the flow behaviour in the wake. In the POD we have used the method described by Sirovich (1987b) to split the original data into two sets: one set that is symmetric with respect to the symmetry plane ($z=0$), and one which is anti-symmetric. This procedure will be described in detail in § 3.1.

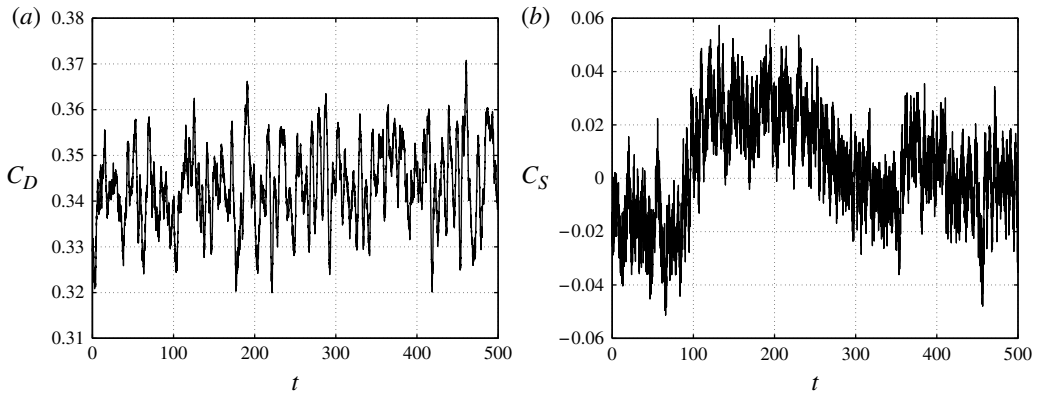


FIGURE 2. Time history of the force signals from the LES of the natural flow: (a) drag force; (b) side force.

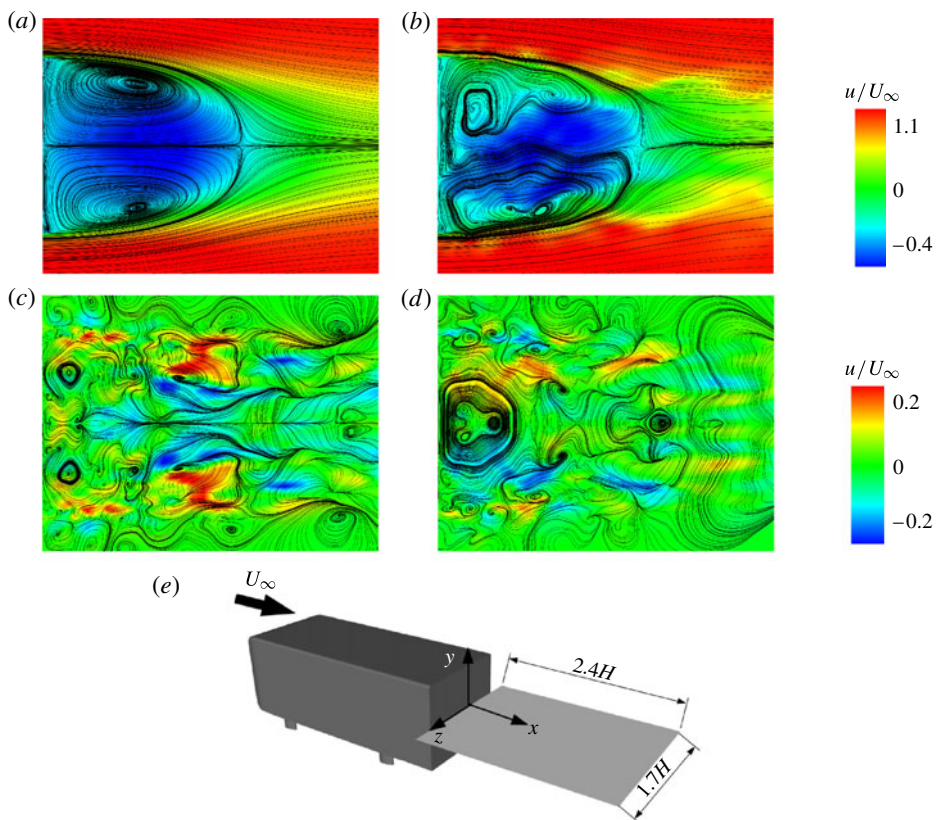


FIGURE 3. (Colour online) Visualizations of the wake flow: (a) time-averaged symmetrized flow; (b) one instantaneous realization; (c) the symmetric part of the instantaneous realization; (d) the anti-symmetric part of the instantaneous realization; (e) the Ahmed model and the plane used to visualize the flow.

Figure 3(a) shows the symmetrized mean flow, $\mathbf{u}(\mathbf{x})$. Figure 3(b) shows one instantaneous realization of the flow and figures 3(c) and 3(d) show the corresponding symmetric and anti-symmetric decomposition of that snapshot, respectively. Here, the mean flow has been subtracted from the symmetric snapshot (the anti-symmetric mean is zero) so that it corresponds to the input of the POD.

3. Reduced order modelling

In this section, the path to the POD model is outlined. In § 3.1, the employed LES data and its symmetrization is outlined. In § 3.2, the POD expansion is described. Finally in § 3.3, the refined subscale turbulence representations are discussed.

3.1. LES snapshots

The POD is based on $M = 1000$ snapshots of the LES. The sampling frequency is two, i.e. 500 convective time units are covered. The convective time unit is based on H and U_∞ . Statistical symmetry with respect to the $z=0$ plane is enforced following Sirovich (1987b). This symmetrization increases the accuracy of the POD decomposition.

Each velocity field is decomposed into a symmetric and antisymmetric contribution with respect to the plane $z = 0$,

$$\mathbf{u}(x, y, z) = \mathbf{u}_s(x, y, z) + \mathbf{u}_{as}(x, y, z). \quad (3.1)$$

Here, the symmetric part \mathbf{u}_s is defined by

$$u_s(x, y, z) = \frac{1}{2}(u(x, y, z) + u(x, y, -z)), \quad (3.2a)$$

$$v_s(x, y, z) = \frac{1}{2}(v(x, y, z) + v(x, y, -z)), \quad (3.2b)$$

$$w_s(x, y, z) = \frac{1}{2}(w(x, y, z) - w(x, y, -z)) \quad (3.2c)$$

while the anti-symmetric component \mathbf{u}_{as} reads

$$u_{as}(x, y, z) = \frac{1}{2}(u(x, y, z) - u(x, y, -z)), \quad (3.3a)$$

$$v_{as}(x, y, z) = \frac{1}{2}(v(x, y, z) - v(x, y, -z)), \quad (3.3b)$$

$$w_{as}(x, y, z) = \frac{1}{2}(w(x, y, z) + w(x, y, -z)). \quad (3.3c)$$

Thus, $M = 1000$ snapshots create equal numbers of symmetric and anti-symmetric snapshots. The POD is performed on each of the symmetrized sets separately. The resulting two PODs are combined in a single POD and sorted according to their energy level. Thus, we have in total 2000 POD modes. This procedure has already been recommended by Sirovich (1987b) and guarantees the expected statistical symmetries of the snapshot ensemble. In addition, the POD modes are either symmetric or anti-symmetric, as derivable from theory.

In principle, the same results can be achieved by a simpler method: the more commonly employed inclusion of M mirror-symmetric snapshots in the snapshot ensemble. However, in practice, pure symmetric and anti-symmetric POD modes are guaranteed only in their corresponding subspace. We observed that some symmetric and anti-symmetric POD modes with very similar energy levels in the first approach yield two non-symmetric (mixed) modes in the second approach due to numerical errors.

3.2. Proper orthogonal decomposition

We perform a POD expansion (Lumley 1970) of M temporally equidistantly sampled velocity snapshots $\mathbf{u}^m := \mathbf{u}(\mathbf{x}, t^m)$ at times $t^m = m\Delta t$, $m = 1, \dots, M$ with the time step Δt . The averaging operation of any velocity-dependent function $\mathbf{F}(\mathbf{u})$ over this ensemble is denoted by angular brackets,

$$\langle \mathbf{F}(\mathbf{u}) \rangle := \frac{1}{M} \sum_{m=1}^M \mathbf{F}(\mathbf{u}^m). \quad (3.4)$$

The colon in front of the sign emphasizes that the left-hand side is defined by the right-hand side of the equation. The observation region $\Omega_{ROM} \subset \Omega$ is a wake-centred subset of the computational domain

$$\Omega_{ROM} = \{(x, y, z) \in \Omega : 0 \leq x \leq 5H, -0.67H \leq y \leq 1.12H, |z| \leq 1.21H\}. \quad (3.5)$$

This domain is large enough to resolve the recirculation region and the absolutely unstable wake dynamics, but small enough to keep the model dimension affordable. The corresponding inner product for two velocity fields $\mathbf{v}, \mathbf{w} \in \mathcal{L}^2(\Omega_{ROM})$ reads

$$(\mathbf{v}, \mathbf{w})_{ROM} := \int_{\Omega_{ROM}} \mathbf{d}\mathbf{x} \mathbf{v} \cdot \mathbf{w}. \quad (3.6)$$

This inner product defines the energy norm $\|\mathbf{v}\|_{ROM} := \sqrt{(\mathbf{v}, \mathbf{v})}$.

The averaging operation and inner product uniquely define the employed snapshot POD (Sirovich 1987a; Holmes *et al.* 2012). First, the velocity field is decomposed into a mean field, $\mathbf{u}_0 = \langle \mathbf{u} \rangle$, and a fluctuating contribution, \mathbf{u}' , following the Reynolds decomposition. Then, the fluctuating part is approximated by a Galerkin expansion with space-dependent modes \mathbf{u}_i , $i = 1, 2, \dots$ and the corresponding mode coefficients $a_i(t)$:

$$\mathbf{u}(\mathbf{x}, t) = \mathbf{u}_0(\mathbf{x}) + \mathbf{u}'(\mathbf{x}, t), \quad (3.7a)$$

$$\mathbf{u}'(\mathbf{x}, t) = \sum_{i=1}^{\infty} a_i(t) \mathbf{u}_i(\mathbf{x}) \approx \sum_{i=1}^N a_i(t) \mathbf{u}_i(\mathbf{x}) + \mathbf{u}_{res}(\mathbf{x}, t). \quad (3.7b)$$

POD yields the minimal average squared residual $\langle \|\mathbf{u}_{res}\|^2 \rangle$ as compared to any other Galerkin expansions with N modes (Lumley 1970). Note that the snapshot POD method limits the number of POD to $N \leq M - 1$. When summing up over $i = 1, 2, \dots$, without bound, we consider the original formulation of POD with an accountable infinity of modes.

We re-write the POD expansion more compactly, following the convention of Rempfer & Fasel (1994a,b):

$$\mathbf{u}(\mathbf{x}, t) = \mathbf{u}_0(\mathbf{x}) + \sum_{i=1}^N a_i(t) \mathbf{u}_i(\mathbf{x}) = \sum_{i=0}^N a_i(t) \mathbf{u}_i(\mathbf{x}), \quad (3.8)$$

where $a_0 \equiv 1$. For later reference, we recapitulate the first and second moments of the POD mode coefficients:

$$\langle a_i \rangle = 0, \quad \langle a_i a_j \rangle = \lambda_i \delta_{ij}. \quad (3.9)$$

The energy content in each mode is given by $K_i(t) = (1/2)a_i(t)^2$. The total turbulence kinetic energy (TKE) resolved by the Galerkin expansion $K_\Sigma(t)$ reads

$$K_\Sigma(t) = \sum_{i=1}^N K_i(t). \quad (3.10)$$

The limit $\lim_{N \rightarrow \infty} K_\Sigma$ for POD yields the TKE K of the velocity field. From here onwards in the paper, the time-averaged value of the quantity K , K_i and K_Σ is implied when the t dependence is dropped, e.g. $K = \langle K(t) \rangle$, $K_i = \langle K_i(t) \rangle$ and $K_\Sigma = \langle K_\Sigma(t) \rangle$. Note that by (3.9), the modal energy and POD eigenvalues are synonymous: $K_i = \lambda_i/2$.

The Galerkin expansion (3.8) satisfies the incompressibility condition by construction. The evolution equation for the mode coefficients a_i is derived by a Galerkin projection onto the NSE (2.1), i.e. from $(\mathbf{u}_i, \mathbf{R}(\mathbf{u}))_{\Omega_{ROM}} = 0$. Details are provided in the textbooks of Noack *et al.* (2011) and Holmes *et al.* (2012). For large domains and three-dimensional fluctuations, the pressure term can generally be neglected as in Deane *et al.* (1991), Ma & Karniadakis (2002) and Noack, Papas & Monkewitz (2005). Here, the Galerkin projection of the pressure term was found to be negligible and it is thus omitted from the model. Thus, the Galerkin system describing the temporal evolution of the modal coefficients, $a_i(t)$, reads

$$\frac{da_i}{dt} = \nu \sum_{j=0}^N l_{ij}^v a_j + \sum_{j,k=0}^N q_{ijk}^c a_j a_k. \quad (3.11)$$

The coefficients l_{ij}^v and q_{ijk}^c are the Galerkin system coefficients describing the viscous and convective Navier–Stokes terms, respectively.

3.3. Hierarchy of low-dimensional Galerkin systems

In this section, subscale turbulence representations for truncated Galerkin systems are revisited. We have to account for the dynamic effect of \mathbf{u}_{res} in (3.7). First, the exact form of the Galerkin system (propagator) residual is detailed (§ 3.3.1). Then, four eddy-viscosity terms for this residual are outlined based on a single constant eddy viscosity (§ 3.3.2), a modal constant eddy viscosity (§ 3.3.3), a single nonlinear eddy viscosity (§ 3.3.4), and a combination of the last two models (§ 3.3.5).

3.3.1. Exact representation of the propagator residual

The dynamical system (3.11) predicts the evolution of all modal coefficients. By integrating the Galerkin system in time we can obtain further long-term information about the dynamical behaviour of the original system. However, the aim is to simulate the dynamical behaviour of the ‘large’ scales that presumably govern the global physics of the flow in the wake of the Ahmed body. This is desirable since the time to compute the convective term, q_{ijk}^c , and the integration time of the system scales as $\sim N^3$, so that the computational effort soon exceeds that of the original LES. Thus, we want to build a ROM that contains the important physics, but with a computational effort to build and to integrate in time that is much less than the time to perform the original LES. We therefore choose a small number of modes N , accounting for the unresolved POD modes at $i = N + 1, N + 2, \dots$ with a subscale

turbulence representation. Let $\mathbf{a} = (a_1, a_2, \dots)$ represent the mode coefficients. Then the accurate dynamical system takes the following form:

$$\frac{da_i}{dt} = f_i(\mathbf{a}) + g_i(\mathbf{a}), \quad (3.12a)$$

$$f_i(\mathbf{a}) = \nu \sum_{j=0}^N l_{ij}^v a_j + \sum_{j,k=0}^N q_{ijk}^c a_j a_k, \quad (3.12b)$$

$$g_i(\mathbf{a}) = \nu \sum_{j=N+1}^{\infty} l_{ij}^v a_j + \sum_{\substack{j,k=0 \\ \max\{j,k\} > N}}^{\infty} q_{ijk}^c a_j a_k. \quad (3.12c)$$

Here, the propagator f_i represents the resolved part of the dynamics while g_i represents the residual of the truncated Galerkin system. This residual contains the viscous and convective terms, with at minimum one unresolved mode $i > N$.

In the Kolmogorov description of the turbulence cascade (Kolmogorov 1941a,b; Pope 2000), the large, energy-carrying scales transfer energy to successively smaller scales where most of the dissipation of the kinetic energy to internal energy (heat) of the molecules takes place. Therefore, any attempt to solve the reduced system in (3.12b) not accounting for the residual, $g_i(\mathbf{a})$, will lead to excessive energy levels, or even divergence of the system.

3.3.2. Single constant eddy viscosity (Galerkin system A)

In the ground-breaking work by Aubry *et al.* (1988) on the dynamics of coherent structures in the turbulent boundary layer, the residual was modelled by a constant ‘eddy viscosity’ term, resulting in a linear subscale turbulence representation $g_i(\mathbf{a}) = \nu_0^T \sum_{j=1}^N l_{ij}^v a_j$. Here ν_0^T is generally obtained by solution matching techniques. In this study, the eddy viscosity is derived from the TKE power balance. The resulting model (3.12) will be called Galerkin system A and abbreviated as GS-A.

3.3.3. Modal constant eddy viscosity (Galerkin system B)

Rempfer & Fasel (1994a) refined the linear model by reasoning that the eddy viscosity should be scale-dependent, resulting in modal eddy viscosities ν_i^T , $i = 1, \dots, N$. The resulting linear subscale turbulence representation reads $g_i(\mathbf{a}) = \nu_i^T \sum_{j=1}^N l_{ij}^v a_j$. Here ν_i^T can be obtained by solution matching. In this study, ν_i^T is derived from the modal power balance (Noack *et al.* 2005). We refer to the resulting model as Galerkin system B, or GS-B.

3.3.4. Single nonlinear eddy viscosity (Galerkin system C)

Noack *et al.* (2011) remark that the subscale turbulence representations of GS-A and GS-B are linear while the energy transfer is caused by nonlinear mechanisms. We start with a single eddy-viscosity ansatz

$$g_i(\mathbf{a}) = \nu_0^T(\mathbf{a}) \sum_{j=1}^N l_{ij}^v a_j, \quad (3.13)$$

but allow the eddy viscosity to be state-dependent. On the other hand (3.13) is written as

$$g_i(\mathbf{a}) = \nu \sum_{j=N+1}^{\infty} l_{ij}^v a_j + \sum_{\substack{j,k=0 \\ \max\{j,k\} > N}}^{\infty} q_{ijk}^c a_j a_k. \quad (3.14)$$

Evidently, both terms cannot be exactly matched. However, the energy transfer rate effect should be similar. In the modal power balance, this energy loss is quantified by $\langle a_i g_i \rangle$. Equality of the energy transfer rate yields

$$v^T l_{ii}^v \lambda_i = \sum_{\substack{j,k=0 \\ \max\{j,k\} > N}}^{\infty} T_{ijk}, \quad \text{where } T_{ijk} = q_{ijk}^c \langle a_i a_j a_k \rangle, \quad (3.15)$$

exploiting $\langle a_i a_j \rangle = \lambda_i \delta_{ij}$ (3.9). The triadic power terms on the right-hand side may be approximated with a FTT closure (Noack *et al.* 2008)

$$T_{ijk} = \alpha \chi_{ijk} \sqrt{K_i K_j K_k} \left(1 - \frac{3K_i}{K_i + K_j + K_k} \right), \quad (3.16)$$

where α and χ_{ijk} are determined from the Galerkin system (see Noack *et al.* 2008).

In the next step, we introduce relative modal energy contents κ_i via $K_i = \kappa_i K_\Sigma$, with $\sum_{i=1}^N \kappa_i = 1$. Then, (3.15) becomes

$$2v^T l_{ii}^v \kappa_i = \sqrt{K_\Sigma} \sum_{\substack{j,k=0 \\ \max\{j,k\} > N}}^{\infty} \alpha \chi_{ijk} \sqrt{\kappa_i \kappa_j \kappa_k} \left(1 - \frac{3\kappa_i}{\kappa_i + \kappa_j + \kappa_k} \right). \quad (3.17)$$

This closure relation suggests that v_T scales with $\sqrt{K_\Sigma}$, assuming that the κ_i remain approximately constant with K_Σ . The resulting nonlinear eddy-viscosity model used in the present work thus takes the form:

$$g_i(\mathbf{a}) = v_0^T \sqrt{\frac{K_\Sigma(t)}{K_\Sigma}} \sum_{j=1}^N l_{ij}^v a_j. \quad (3.18)$$

Thus, large (small) fluctuation levels $K_\Sigma(t) > K_\Sigma$ ($K_\Sigma(t) < K_\Sigma$) lead to a higher (smaller) damping than predicted by the corresponding linear subscale turbulence representation. In particular, boundedness of the new Galerkin system C (GS-C) can be proved, if the energy preservation of the quadratic term is enforced (Cordier *et al.* 2013).

3.3.5. Modal nonlinear eddy viscosity (Galerkin system D)

Combining the nonlinear eddy viscosity of GS-C (3.18) and the modal eddy viscosities of GS-B yields the following nonlinear subscale turbulence representation:

$$g_i(\mathbf{a}) = v_i^T \sqrt{\frac{K_\Sigma(t)}{K_\Sigma}} \sum_{j=1}^N l_{ij}^v a_j. \quad (3.19)$$

The resulting dynamical system is referred to as Galerkin system D, or GS-D.

4. Results

In this section, we present results of the four Galerkin systems A–D from §§3.3.2–3.3.5, respectively. First, the POD is presented (§4.1). Then, the solutions of Galerkin systems A–D are compared (§4.2). Finally, the robustness of the Galerkin systems in terms of model parameters is investigated (§4.3).

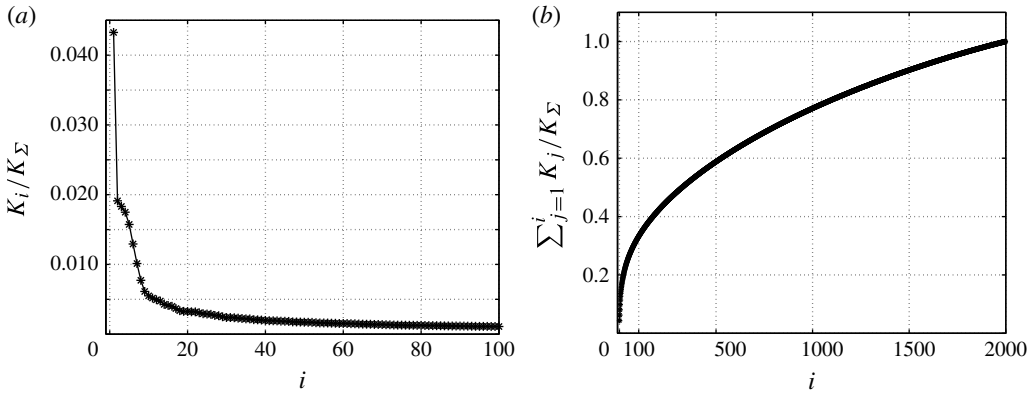


FIGURE 4. Spectrum from the POD: (a) Normalized spectrum; (b) Normalized cumulative spectrum. The first mode has by far the largest energy level. It resolves asymmetric base-flow variations between positive and negative side forces.

4.1. POD

Figure 4 presents the cumulative spectrum from the POD eigenvalues of the dataset of flow snapshots during the considered time interval. The convergence rate is quite slow, and the first 100 modes contain some 35 % of the total kinetic energy in the system. The first 500 modes resolve 60 % of the kinetic energy. We will not visualize the POD modes here, as their structure contributes little to the understanding of the subscale turbulence representations. It is only important to note that the first POD mode \mathbf{u}_1 describes a slow base-flow change between positive and negative side forces. This mode is called the shift mode (Noack *et al.* 2003), reflecting the analogous role in resolving base flow changes.

4.2. Comparative study of the Galerkin systems

The key parameters of the subscale turbulence representation are the total and modal eddy viscosities of Galerkin systems A and B, respectively. These parameters have been determined by the total and modal power balance for GS-A and GS-B, respectively. In other words, no solution matching is performed. Figure 5 shows their values. The total eddy viscosity ν_0^T lies between the extremal modal values, as expected. The modal eddy viscosities ν_i^T are all positive and follow a nearly monotonous trend with the mode index i . Such a nearly monotonous behaviour indicates a good quality of the LES data. For other flow data, the authors frequently observe a large scatter of these values with i .

Galerkin system C (GS-C) assumes the ν_0^T of GS-A and rescales the value according to the square-root law (3.18). Similarly, GS-D applies the same scaling to the modal eddy viscosities ν_i^T of GS-B.

We start the comparison of the four Galerkin systems with the modal energy spectrum K_i of their respective long-term solutions. From figure 6, the most simple GS-A is seen to deviate farthest from the CFD values. Better spectra might be obtained with solution matching techniques for ν_0^T (see below), but such a procedure indicates that the total power balance as a consistency condition is violated.

GS-B indicates an increased performance on replacing the total eddy viscosity by the modal analogues. The increase in employed knowledge from the NSE, namely the use of N modal power balances, pays off.

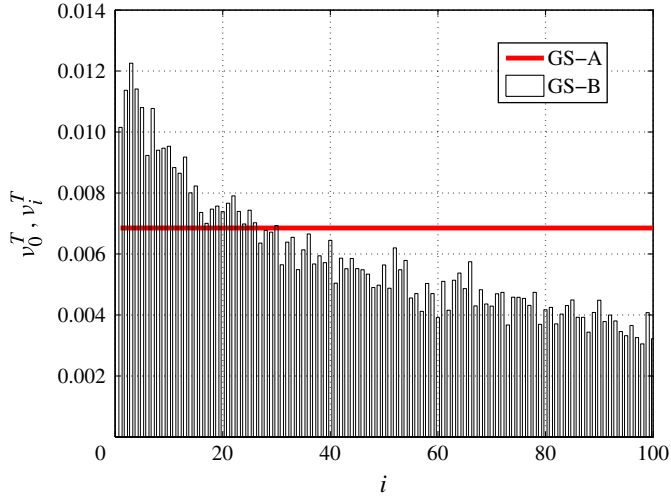


FIGURE 5. (Colour online) Total and modal eddy viscosities of Galerkin systems A and B.

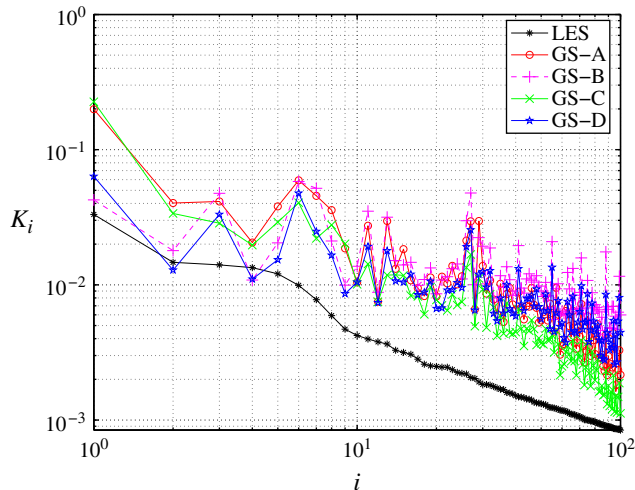


FIGURE 6. (Colour online) Comparison of the modal kinetic energies K_i between the LES and the four Galerkin system solutions (GS-A...D).

GS-C tends to outperform both Galerkin systems, particularly for large mode indices. This indicates that the nonlinearity of the eddy-viscosity ansatz is a crucial physical enabler and should not be ignored. The correct TKE-dependent scaling of the eddy viscosity appears to be more important than the modal refinement of their values. However, one should note that the deviation of the modal eddy-viscosity values from the total analogue is less than a factor two for this particular flow. The energy levels in mode one (the shift mode) and the oscillatory modes $i = 2, \dots, 11$ are over-predicted by GS-C as compared to the levels of the LES. One reason for this over-prediction is a shortcoming of the total eddy viscosity: the physically

correct modal values for these modes are almost two times larger. Similarly, the next (large-scale) oscillatory POD modes $i=2, \dots, 7$ are over-predicted.

Galerkin system D has larger eddy viscosities for the most dominant first POD modes and cures the over-prediction of the corresponding modal amplitudes of GS-C. The modal energies of the higher-order modes of GS-B and GS-D are comparable. The modal refinement of the nonlinear eddy-viscosity term has a price: the higher-order (less energetic) modes of GS-D tend to be more energetic than the those of GS-C. We hypothesize that the cause is a broadband frequency time-variation of the eddy viscosity due to $K_{\Sigma}(t)$. The modal eddy viscosities of the higher-order modes are smaller than the total eddy viscosity (see figure 5). Hence, the higher-order modes of GS-D are less damped and more energized by the unsteady subscale turbulence term as compared to GS-C. A low-pass filter on $K_{\Sigma}(t)$ could cure this problem, if the low-energy tail of the POD decomposition is of sufficient interest. We will not incorporate this additional refinement here.

The temporal dynamics of the GS-D and the POD (from LES data) are presented for selected modes in figure 7. The first coefficient a_1 of the shift mode is the most interesting one. This coefficient is depicted in figure 7(a) and describes the change from one asymmetric base-flow state to the other. Its value follows exactly the side-force signal from the LES in figure 2(b). Only Galerkin system D was found capable of predicting the sudden switches from one side force state to the other with realistic amplitudes at realistic time scales. Also GS-C exhibits such base-flow changes, but the amplitude is over-predicted by a factor two and these time scales were over-predicted by three orders of magnitudes. GS-A predicts a purely periodic solution for $N=100$, and GS-B does not predict the amplitude in a physical correct way. Summarizing, both the modal refinement of the eddy viscosity (GS-B and GS-D) and their energy-dependent scaling in (GS-C and GS-D) emerge as crucial enablers for the accurate Galerkin systems.

4.3. Robustness study of the Galerkin systems

In this section, the robustness of the Galerkin systems with respect to their dimension and the eddy-viscosity parameters is investigated.

In figure 8, the time-averaged total energy of all Galerkin systems is depicted for different dimensions N of the ROM. GS-D has, on average, the best agreement with the LES values for all four dimensions, i.e. $N=10, 20, 50$ and 100 . In contrast, the most simple GS-A shows even the wrong trend with respect to N . We emphasize that all eddy-viscosity values are derived from TKE power balances. The performance of each Galerkin system could easily be improved with solution matching techniques for these parameters. However, the price of such techniques is a potentially large residual in the TKE power balance, i.e. the predicted modal energy distribution and energy flows may be significantly distorted.

Finally, the role of the eddy-viscosity parameter is investigated in figure 9 for $N=100$. For the simulations in this figure, we have varied the total viscosities ν_i^T in the range 25, 50, 75, 150, 200, 250 and 300 % of the reference value ν_0^T for GS-A and GS-C. The modal eddy viscosities ν_i^T of GS-B and GS-D have been changed by the same factor depicted on the abscissa. GS-A does not show monotonous behaviour in terms of the parameter change. GS-B has a more monotonous physical behaviour but its deviations are stronger than for GS-A. One may speculate that modal eddy viscosities are ‘over-fitted’ for the physical reference level. GS-C is seen to be far less affected by these changes, the nonlinear eddy viscosity compensates for too small or too large

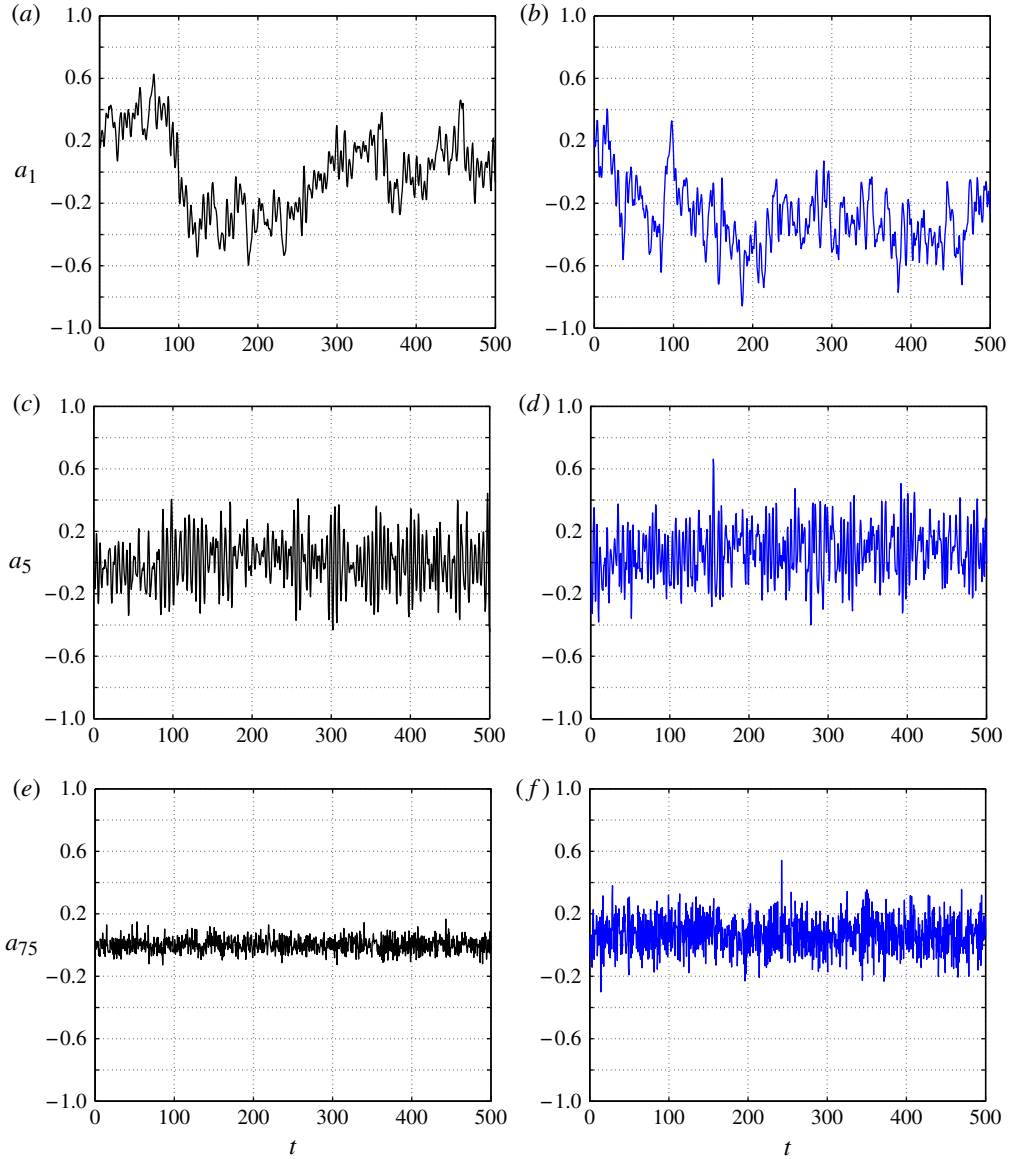


FIGURE 7. (Colour online) Evolution of the mode coefficients $a_i(t)$. Comparison between LES (a,c,e) and GS-D (b,d,f) for $N = 100$. (a,b) $a_1(t)$, describing asymmetric base flow changes (shift mode); (c,d) $a_5(t)$, as an example of a dominant oscillatory POD mode; (e,f) $a_{75}(t)$, representing a higher-order POD mode.

reference values. Finally, GS-D follows GS-C but shows an even smoother curve, thus indicating the largest robustness.

Finally, in figure 10 we present the temporal evolution of the total energy level for all four Galerkin systems for dimensions $N = 20$, $N = 50$, $N = 100$. The systems with dimensions $N = 20$ and $N = 50$ are pure truncations of the $N = 100$ reference. This implies that the eddy viscosities of the $N = 100$ reference are kept constant in this system reduction. We do not want to mix the effect of varying dimensions and

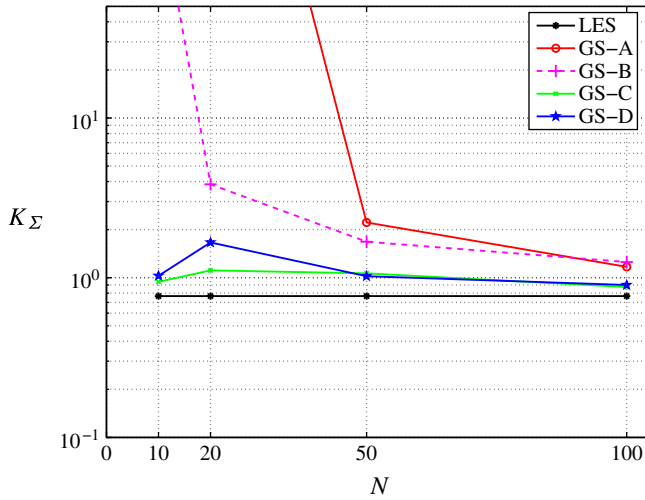


FIGURE 8. (Colour online) Comparison of the total energy, K_Σ , in the ROM for different dimensions N of the ROM. The eddy viscosity is kept constant to the value of that for $N = 100$.

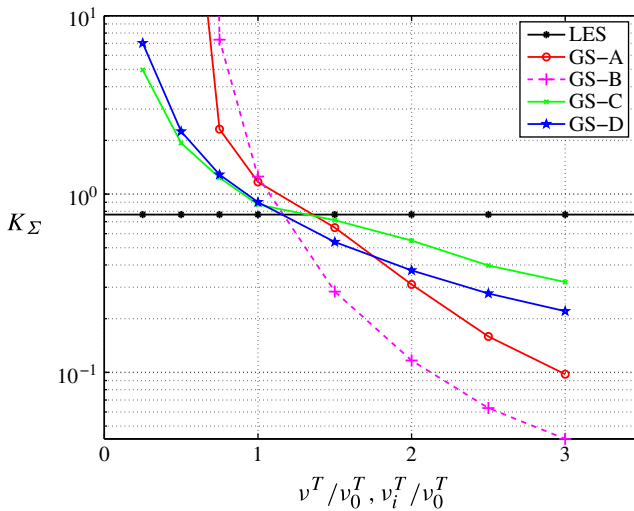


FIGURE 9. (Colour online) Comparison of the total energy, K_Σ , in the ROM for different values of v_i^T and v_0^T .

varying eddy viscosity. Again, GS-C and GS-D with the nonlinear subscale turbulence representation outperform GS-A and GS-B in terms of robustness.

Mean values and the variances of the signals from the $N = 100$ ROMs (see figure 10) and LES are presented in table 1. GS-C predicts the mean value slightly closer to LES than GS-D, but the variance of GS-C (0.0304) is overpredicted by a factor of three compared to the LES (0.0095), while the variance of GS-D (0.0091) is close to that of the LES. GS-A and GS-B overpredict the mean and variance significantly.

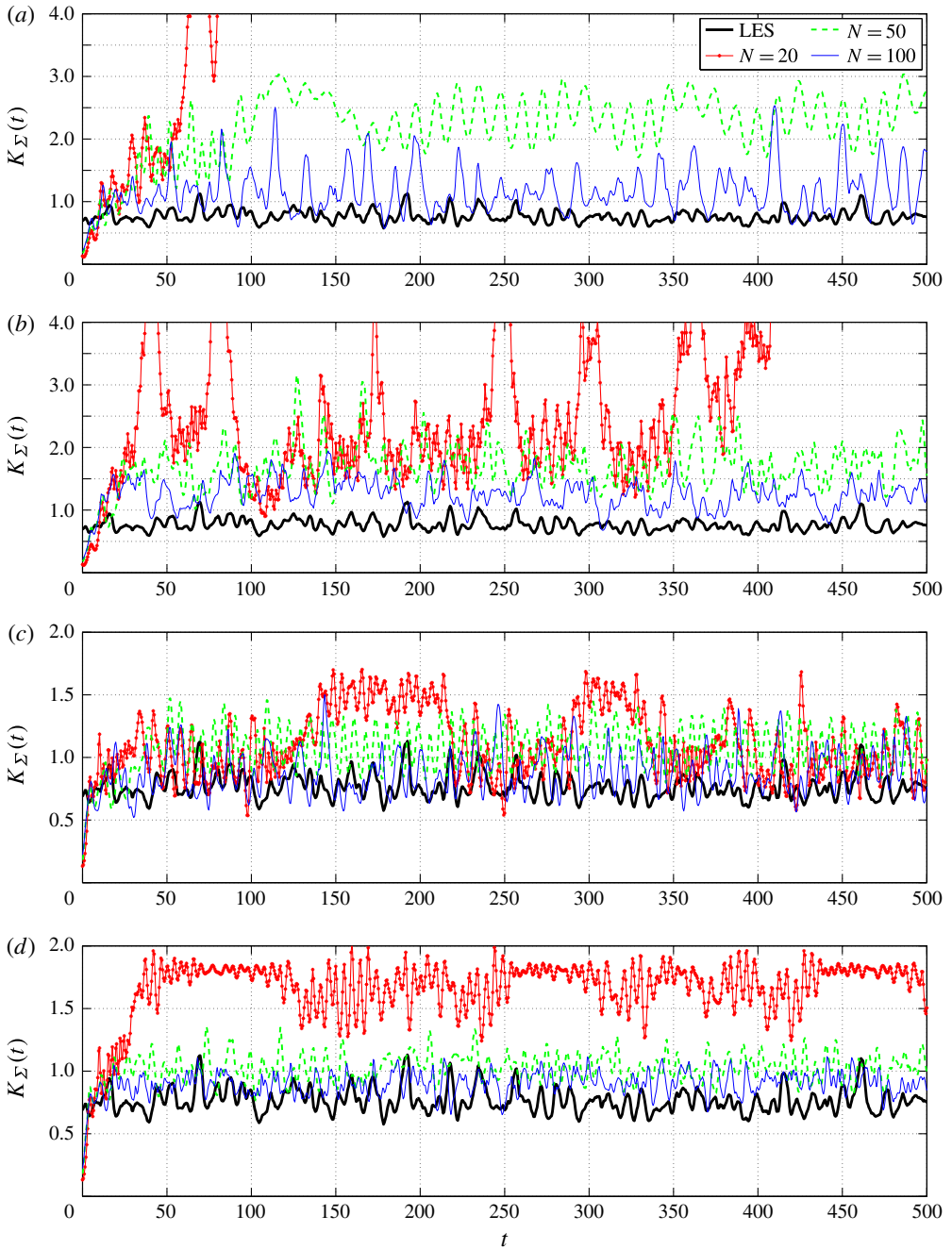


FIGURE 10. (Colour online) Comparison of instantaneous total energy $K_\Sigma(t) = \sum_{i=1}^N K_i(t)$ of the Galerkin systems: (a) GS-A; (b) GS-B; (c) GS-C; (d) GS-D. Note that the scaling of the y-axis between figures (b) and (c) is different.

	GS-A	GS-B	GS-C	GS-D	LES
Mean	1.1693	1.2535	0.8740	0.9010	0.7671
Variance	0.1264	0.0606	0.0304	0.0091	0.0095

TABLE 1. Mean values and variances of $K_{\Sigma}(t)$ for the $N = 100$ ROMs and LES.

In summary, the accuracy and robustness of the Galerkin system is found to improve by modal refinement of the eddy viscosities and by an energy-dependent scaling. A similar observation for the energy-dependent scaling has been made for the POD models of a mixing layer by Cordier *et al.* (2013).

5. Conclusions

We have investigated a hierarchy of linear and nonlinear eddy-viscosity terms for a POD Galerkin model accounting for the unresolved velocity fluctuations. The chosen configuration is a high-Reynolds-number flow over a square-back Ahmed body. This flow exhibits three challenging features for reduced-order models. Firstly, the high Reynolds number implies that a subscale turbulence representation is mandatory for realistic fluctuation levels, or even boundedness, of the Galerkin system solution. Secondly, the coherent structures of the Ahmed body have a broadband frequency signature. The resulting frequency cross-talk implies that many modal interactions exist and need to be correctly resolved. Thirdly, the base flow has two meta-stable states with nearly constant non-vanishing side forces. Experiments on a similar Ahmed body configuration (Grandemange *et al.* 2013) exhibit these asymmetric quasi-attractors. Such quasi-attractors imply a complex interaction from small to very large time scales and constitute a significant modelling challenge – even for Navier–Stokes simulations.

The solutions of a POD Galerkin model with 100 modes or less converge to infinity, underlining the need for a subscale turbulence presentation. Four corresponding auxiliary models have been tested, using a single or modally refined eddy viscosities with constant or energy-dependent values. These parameters are determined from the total or modal TKE power balance. Solution matching techniques are excluded as a parameter identification method, to avoid any inconsistency with the TKE power balances. A single constant eddy viscosity, as used by Aubry *et al.* (1988) and others, is already sufficient to stabilize the Galerkin solution. Modally refined viscosities, as suggested by Rempfer & Fasel (1994b), are found to significantly improve the accuracy of the modal fluctuation energies. However, both approaches rely on constant eddy viscosities, leading to linear subscale turbulence representations for nonlinear energy flow cascade. The resulting Galerkin solutions converge to infinity if the initial conditions are far from the attractor. In addition, neither Galerkin system exhibits the meta-stable asymmetric base flow states.

We corroborate the need for eddy viscosities which scale with the square root of the resolved fluctuation energy. The single nonlinear eddy-viscosity model leads to an accurate prediction for the fluctuation levels of higher-order modes, while the amplitudes of the first seven modes are over-predicted. Arguably, the first seven modes define the large-scale coherent structures and are the most important part of the spectrum. The modally refined eddy viscosity cures this over-prediction at the expense of a less accurate tail of the modal energy spectrum. These nonlinear eddy-viscosity models are capable of resolving the flipping between asymmetric base flow states.

Constant eddy viscosity (GS-A)

- blow up in finite time for certain initial conditions
- significant overprediction of fluctuation levels (with NSE inferred eddy viscosity)

Modal eddy viscosities (GS-B)

- blow up in finite time for certain initial conditions
- + more accurate prediction of fluctuation levels
- + reduced dependency on ROM dimension N

Nonlinear constant eddy viscosity (GS-C)

- significant overprediction of fluctuation levels
- + guaranteed boundedness of solution, independent of the initial condition
- + reduced dependency on ROM dimension N
- + reduced dependency on v_T variation

Nonlinear modal eddy viscosity (GS-D)

- + guaranteed boundedness of solution, independent of the initial condition
- + more accurate prediction of fluctuation levels
- + reduced dependency on ROM dimension (N)
- + reduced dependency on v_T variation

TABLE 2. Performance of the Galerkin systems A–D: ‘–’ refers to challenges, ‘+’ to improvements with respect to the benchmark Galerkin system A.

In addition, the resulting Galerkin systems converge to their respective attractors for initial conditions – even if these are far away from them. Global convergence can be strictly ensured by enforcing energy preservation on the quadratic term. This energy preservation is derivable from the NSE (Kraichnan & Chen 1989; Schlegel & Noack 2013). In addition, Galerkin systems with nonlinear subscale turbulence representations are shown to be much more robust with respect to changes of the eddy-viscosity parameters and the dimension of the model.

The modally refined, nonlinear eddy-viscosity terms have significantly increased accuracy and robustness of the Galerkin system as compared to traditional linear subscale turbulence representations. The accuracy has been achieved with a parameter identification, based purely on NSE-based constraints and without solution matching techniques. The robustness is a key enabler for three ROM-based applications. Firstly, the ROM may serve as a test-bed for understanding of the nonlinear dynamics. One key question is the mechanism for the amplitude selection, i.e. what drives the transients towards the attractor. Secondly, the ROM may be employed as a computationally inexpensive surrogate model for multiple purposes, e.g. for the inlet conditions of the flow around a following car model. In this case, it is desirable to have a ROM which works over a certain range of operating conditions, e.g. slowly varying oncoming velocity. This variability implies that the ROM employs a physically correct robust amplitude selection mechanism, e.g. does not diverge for a small change of the Reynolds number. Finally, model-based control design requires a ROM which works robustly for a range of natural and forced transients. Moreover, the control design is often based on a hierarchy of ROMs with different dimensions – ranging from robust least-order models to more accurate higher-order models, which pose greater challenges to state estimation. The nonlinear eddy-viscosity term serves all three mentioned applications. Table 2 summarizes the benefits achieved from the modal and nonlinear eddy-viscosity refinements.

To conclude, the proposed nonlinear subscale turbulence term with modal eddy viscosity of Rempfer & Fasel (1994b) and energy-dependent scaling of Noack *et al.* (2011) is a recipe for accurate and robust POD models for a large class of complex flows, comprising the flow over an Ahmed body as shown here, a mixing layer (Cordier *et al.* 2013), and subsonic jet noise (Schlegel *et al.* 2009). The study emphasizes the decisive role of a good structure identification of the Galerkin system propagator – here in form of a nonlinear stabilizing term – before parameter identification methods are to be applied.

Acknowledgements

The thesis of J. Östh is supported financially by Trafikverket (Swedish Transport Administration). The thesis of D. Barros is supported financially by PSA Peugeot Citroën and ANRT in the context of the OpenLab Fluidics between PSA and Institute PPRIME. The work by S. Krajnović in this paper was partially funded by the Chalmers Sustainable Transport Initiative. The authors acknowledge the funding and excellent working conditions of the Senior Chair of Excellence ‘Closed-loop control of turbulent shear flows using reduced-order models’ (TUCOROM), supported by the French Agence Nationale de la Recherche (ANR) and hosted by Institute PPRIME. We thank the Ambrosys Ltd. Society for Complex Systems Management, the Bernd Noack Cybernetics Foundation and OpenLab PPRIME/PSA for additional support. We appreciate valuable stimulating discussions with our collaborators Markus Abel, Jean-Paul Bonnet, Steven Brunton, Laurent Cordier, Joël Delville, Thomas Duriez, Fabien Harambat, Eurika Kaiser, Robert Niven, Tamir Shaqarin, Vladimir Parezanovic, Bartek Protas, Tony Ruiz, Michael Schlegel, Marc Segond and Andreas Spohn. Special thanks are due to Nadia Maamar for a wonderful job in hosting the TUCOROM visitors.

Software licenses for AVL Fire were provided by AVL List GmbH. Computations were performed at SNIC (Swedish National Infrastructure for Computing) at the Center for Scientific Computing at Chalmers (C3SE), Center for High Performance Computing at KTH (PDC) and National Supercomputer Center (NSC) at LiU.

Last but not least, we thank the referees for their constructive suggestions.

Appendix A. Comparison between experimental data and LES data

This appendix describes the companion experiment at Institute PPRIME, which serves as a reference for the LES. PIV and hot-wire data are used only to validate the data obtained from the LES.

A.1. Description of the experimental set-up

The experiments were conducted in a closed-loop wind tunnel with a test section of 6.24 m². The model was mounted over an elliptical leading-edge flat plate, as illustrated in figure 11. At the end of the flat plate, an inclined flap was adjusted in order to obtain an upstream flow aligned perpendicularly to its leading edge. This procedure was done without the bluff body in the wind tunnel. Considering the upper area above the plate, the blockage ratio is approximately 2% and no blockage corrections were performed. The upstream velocity, measured on the upper surface of the wind tunnel (above the model), was kept constant at $U_\infty = 15 \text{ m s}^{-1}$. Particle image velocimetry (PIV) was performed on the near-wake (see detail in figure 11). Streamwise and transverse (respectively x and y directions) components of

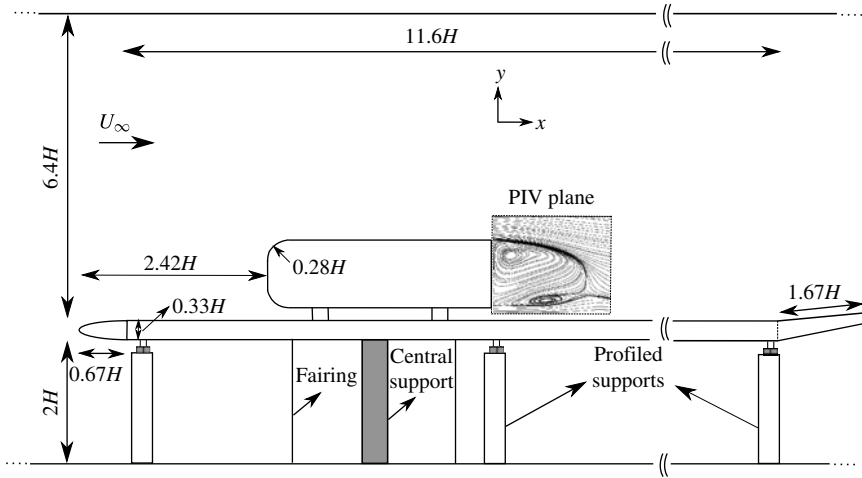


FIGURE 11. Experimental set-up.

the velocity field were measured using two LaVision Imager pro X 4M (resolution 2000×2000 pixels) cameras. A laser sheet was pulsed (with time delays of $120 \mu\text{s}$) in the symmetry plane of the configuration and image pairs were acquired at a sampling frequency of 3 Hz. Velocity vector calculations are processed with an interrogation window of 32×32 pixels (an overlap of 50 %) giving a spatial resolution of approximately 1 % of the model height. Starting with an absolute displacement error of 0.1 pixels, the maximum uncertainty on instantaneous velocity fields is estimated to be 0.2 m s^{-1} . The mean flow was computed using 500 independent velocity fields and the estimated statistical error for time-averaged velocity is $0.09\sigma_{rms}$ with 95 % of confidence level and σ_{rms} is the local root mean square of the velocity.

A.2. Velocity profiles

Figure 12 presents a comparison between the LES results and the experimental data for the time-averaged streamwise velocity component, u , at different locations in the symmetry plane of the wake. The shear layer profile slightly downstream ($0.03H$) of the top trailing edge of the PIV data and the LES data are presented in figure 12(a). The two profiles are in good agreement. The slow recovery of the shear layer is due to momentum loss in the separation on the front edges of the body. Such slow recovery of the shear layer profile at the trailing edge was also found in the experimental study by Grandemange *et al.* (2013). Figures 12(b)–(f) present profiles along lines extending from the ground to a position above the wake at five different streamwise locations in the wake. None of the profiles shows any significant discrepancy between the LES and the PIV data.

A.3. Streamlines of time-averaged velocity in the symmetry plane

Figures 13(a) and 13(b) present the time-averaged flow in the symmetry plane from the PIV data and the LES. The upper centre of the time-averaged toroidal vortical structure in the wake is located closer to the base than the lower centre. The organization of the flow in the wake is very sensitive to the set-up, in particular the

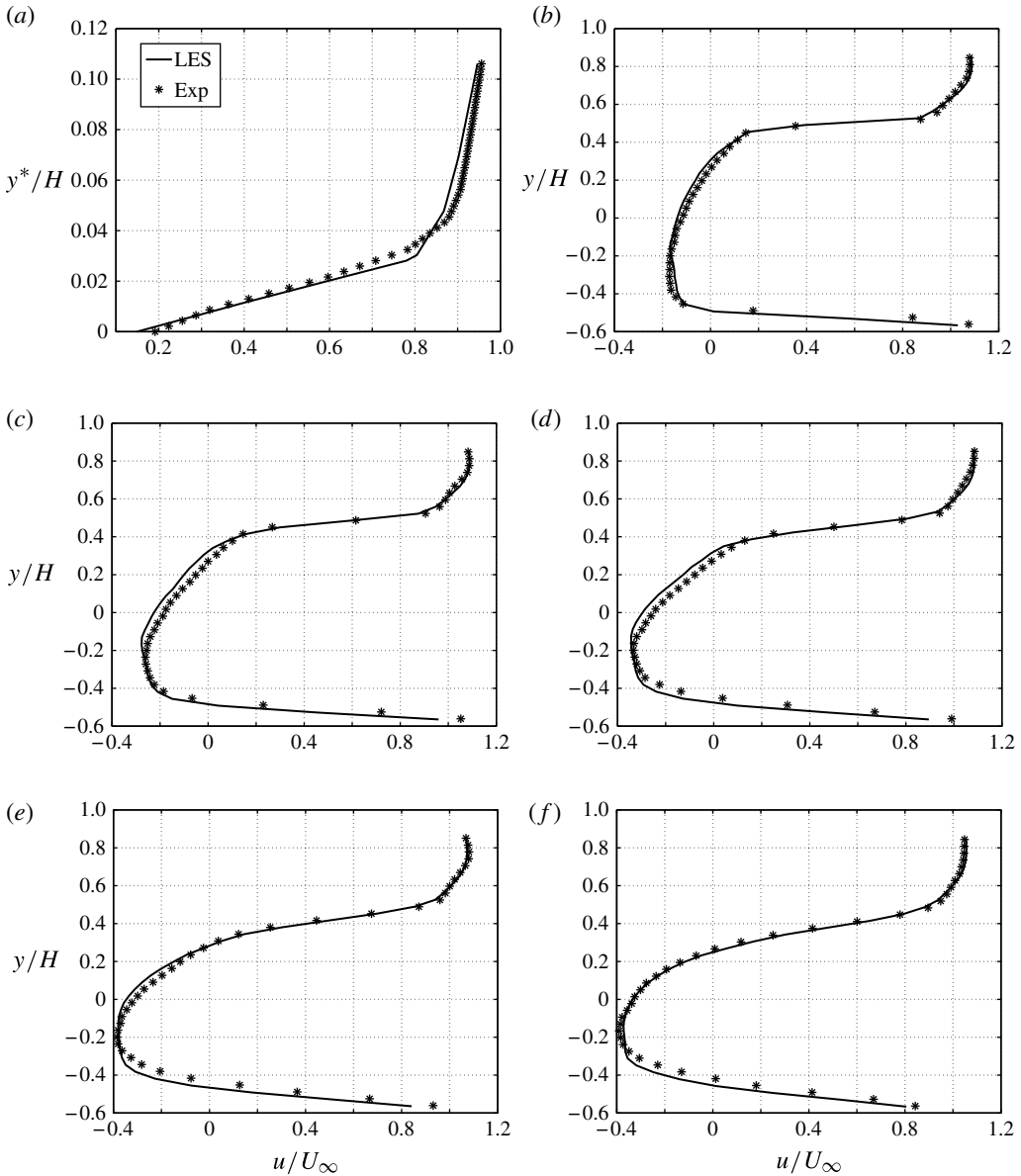


FIGURE 12. Profiles showing comparison of the time-averaged streamwise velocity component, u , for different locations in the wake. (a) Shear layer profile $0.03H$ downstream of the top trailing edge. Here $y^* = y + 0.5H$. (b) $0.17H$ downstream; (c) $0.34H$ downstream; (d) $0.5H$ downstream; (e) $0.67H$ downstream; (f) $0.84H$ downstream.

gap clearance between the body and the ground. Therefore, similar studies of the geometry show different organization of the wake. In the study by Grandemange *et al.* (2013), the location of the upper vortical centre is located further downstream, at the same distance from the base as the lower centre. However, both the gap width and the Reynolds number were less in that study than presented here. Figures 13(c) and 13(d) show one instantaneous realization from the PIV and LES data, respectively.

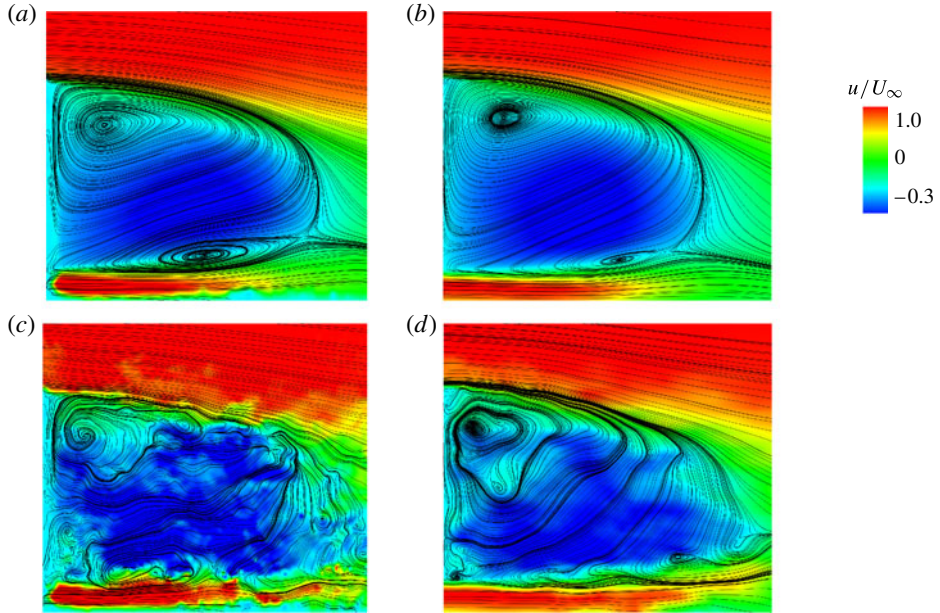


FIGURE 13. (Colour online) Comparison between experimental PIV data and LES data in the symmetry plane. (a) time-averaged PIV; (b) time-averaged LES; (c) one instantaneous realization of PIV data; (d) one instantaneous realization of LES data. The length of the planes is $1.7H$ and the height is $1.5H$.

$mean(\Delta n^+)$	$mean(\Delta x^+)$	$mean(\Delta s^+)$
0.55	80	20

TABLE 3. Spatial resolution in the LES.

A.4. Spectra of the transverse velocity component

Spectra of velocity are presented in figure 14 at a point located downstream of the separation region. Both the hot-wire data and the LES data show a signature at $St \approx 0.2$, corresponding to the global shedding of the wake. This peak was also found in the study by Lahaye, Leroy & Kourta (2014).

Appendix B. Spatial resolution in the LES

The time-averaged spatial resolution on the body expressed in viscous wall units, $\Delta n^+ = \Delta n/\lambda^+$, $\Delta x^+ = \Delta x/\lambda^+$ and $\Delta s^+ = \Delta s/\lambda^+$, is presented in table 3. Here Δn , Δx and Δs refer to the sizes of the cells in the wall-normal direction, streamwise direction and spanwise direction, respectively. Here λ^+ is the viscous length scale, defined as $\lambda^+ = \nu/u^*$, where u^* is the wall friction velocity. The size of the cells in the normal direction on the body, n^+ , is everywhere less than 1. The spatial- and time-average of the viscous length scale on the body, λ^+ , was computed to be $0.0002H$. The values presented in table 3 refer to the mean values on the body.

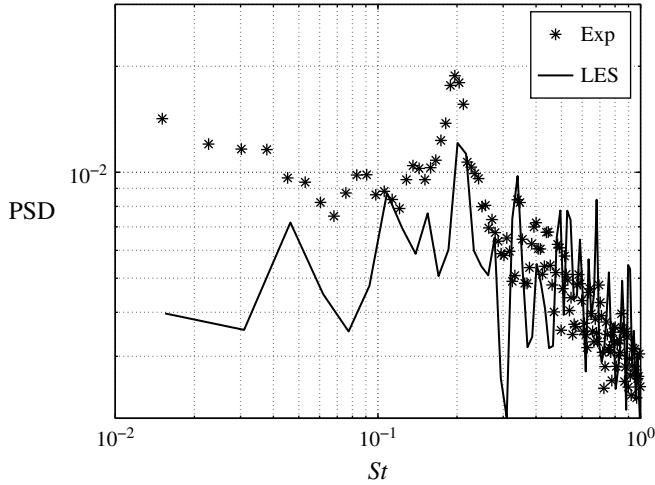


FIGURE 14. Power spectral density (PSD) of the transverse velocity component, v , at the point $x=2.25H$, $y=0.34H$, of LES data and the velocity magnitude of the hot-wire data.

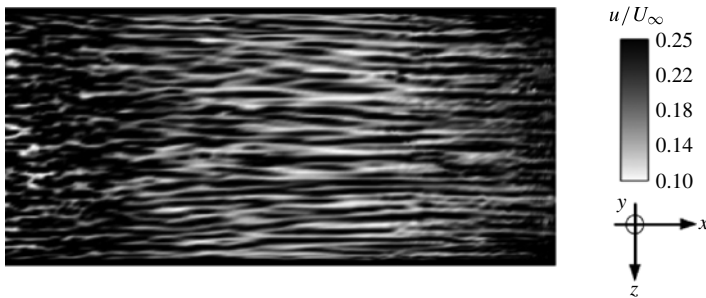


FIGURE 15. A plane cut from the LES in the fifth cell layer away from the roof at approximately $y/\lambda^+ \approx 5$, showing regions of low- and high-speed streamwise velocities. The length of the plane is approximately $13000\lambda^+$ ($2.7H$).

Figure 15 shows the streamwise velocity component in a plane cut in the inner boundary layer on the roof. The figure reveals low- and high-speed streaks in the streamwise direction, indicating the high spatial resolution in the LES.

REFERENCES

- AHMED, S., RAMM, G. & FALTIN, G. 1984 Some salient features of the time-averaged ground vehicle wake. *SAE Tech. Rep.* 840300.
- AIDER, J.-L., BEAUDOIN, J.-F. & WESFREID, J. E. 2010 Drag and lift reduction of a 3D bluff-body using active vortex generators. *Exp. Fluids* **48**, 771–789.
- AUBRY, N., HOLMES, P., LUMLEY, J. L. & STONE, E. 1988 The dynamics of coherent structures in the wall region of a turbulent boundary layer. *J. Fluid Mech.* **192**, 115–173.
- AVL Fire 2013 *CFD Solver. FIRE CFD Solver Users Guide*, v2013.
- BALAJEWICZ, M. J., DOWELL, E. H. & NOACK, B. R. 2013 Low-dimensional modelling of high-Reynolds-number shear flows incorporating constraints from the Navier–Stokes equation. *J. Fluid Mech.* **729**, 285–308.

- BEAUDOIN, J.-F. & AIDER, J.-L. 2008 Drag and lift reduction of a 3D bluff body using flaps. *Exp. Fluids* **44**, 491–501.
- BOBERG, L. & BROSA, U. 1988 Onset of turbulence in a pipe. *Z. Naturforsch.* **43a**, 697–726.
- BRUNN, A., NITSCHKE, W., HENNING, L. & KING, R. 2008 Application of slope-seeking to a generic car model for active drag control. *AIAA Paper* 2008-6734.
- BUSSE, F. H. 1991 Numerical analysis of secondary and tertiary states of fluid flow and their stability properties. *Appl. Sci. Res.* **48**, 341–351.
- CAZEMIER, W., VERSTAPPEN, R. W. C. P. & VELDMAN, A. E. P. 1998 Proper orthogonal decomposition and low-dimensional models for driven cavity flows. *Phys. Fluids* **10**, 1685–1699.
- CORDIER, L., NOACK, B. R., TISSOT, G., LEHNASCH, G., DELVILLE, J., BALAJEWICZ, M., DAVILLER, G. & NIVEN, R. K. 2013 Identification strategies for model-based control. *Exp. Fluids* **54** (8), 1–21.
- DAVIDSON, L. 2010 How to estimate the resolution of an LES of recirculating flow. In *Quality and Reliability of Large-Eddy Simulations II* (ed. M. V. Salvetti, B. Geurts, J. Meyers & P. Sagaut), Ercoftac Series, vol. 16, pp. 269–286. Springer.
- DEANE, A. E., KEVREKIDIS, I. G., KARNIADAKIS, G. E. & ORSZAG, S. A. 1991 Low-dimensional models for complex geometry flows: application to grooved channels and circular cylinders. *Phys. Fluids A* **3**, 2337–2354.
- DUELL, E. G. & GEORGE, A. R. 1999 Experimental study of a ground vehicle body unsteady near wake. *SAE Paper* 1999-01-0812.
- GALLETTI, G., BRUNEAU, C. H., ZANNETTI, L. & IOLLO, A. 2004 Low-order modelling of laminar flow regimes past a confined square cylinder. *J. Fluid Mech.* **503**, 161–170.
- GRANDEMANGE, M., GOHLKE, M. & CADOT, O. 2013 Turbulent wake past a three-dimensional blunt body. Part 1. Global modes and bi-stability. *J. Fluid Mech.* **722**, 51–84.
- HEMIDA, H. 2008 Numerical simulations of flows around trains and buses in cross winds. PhD thesis, Chalmers University of Technology, Gothenburg, Sweden, ISBN/ISSN 978-91-7385-187-9.
- HEMIDA, H., GIL, N. & BAKER, C. 2010 LES of the slipstream of a rotating train. *Trans. ASME J. Fluids Engng* **132** (5), 051103–051103-9.
- HEMIDA, H. & KRAJNOVIĆ, S. 2008 LES study of the influence of a train-nose shape on the flow structures under cross-wind conditions. *Trans. ASME J. Fluids Engng* **130** (9), 091101–091101-12.
- HEMIDA, H. & KRAJNOVIĆ, S. 2010 LES study of the influence of the nose shape and yaw angles on flow structures around trains. *J. Wind Engng Ind. Aerodyn.* **98**, 34–46.
- HOLMES, P., LUMLEY, J. L., BERKOOZ, G. & ROWLEY, C. W. 2012 *Turbulence, Coherent Structures, Dynamical Systems and Symmetry*, 2nd edn. Cambridge University Press.
- JOSEPH, D. D. 1976 *Stability of Fluid Motions I & II*. Springer-Verlag.
- KOLMOGOROV, A. N. 1941a Dissipation of energy in locally isotropic turbulence. *Dokl. Akad. Nauk SSSR* **32**, 16–18 (translated and reprinted 1991 in *Proc. R. Soc. Lond. A* **434**, 15–17).
- KOLMOGOROV, A. N. 1941b The local structure of turbulence in incompressible viscous fluid for very large Reynolds number. *Dokl. Akad. Nauk SSSR* **30**, 9–13 (translated and reprinted 1991 in *Proc. R. Soc. Lond. A* **434**, 9–13).
- KRAICHNAN, R. H. & CHEN, S. 1989 Is there a statistical mechanics of turbulence? *Physica D* **37**, 160–172.
- KRAJNOVIĆ, S. 2002 Large-Eddy Simulation for computing the flow around vehicles. PhD thesis, Chalmers University of Technology, Gothenburg, Sweden, ISBN/ISSN 91-7291-188-3.
- KRAJNOVIĆ, S. 2009 LES of flows around ground vehicles and other bluff bodies. *Phil. Trans. R. Soc. A* **367** (1899), 2917–2930.
- KRAJNOVIĆ, S. 2011 Flow around a tall finite cylinder explored by large eddy simulation. *J. Fluid Mech.* **676**, 294–317.
- KRAJNOVIĆ, S. 2013 LES investigation of passive flow control around an Ahmed body. In *ASME 2013 International Mechanical Engineering Congress & Exposition, San Diego, CA, USA*, vol. 1, pp. 305–315, Paper IMECE2013-62373.
- KRAJNOVIĆ, S. & DAVIDSON, L. 2003 Numerical study of the flow around the bus-shaped body. *Trans. ASME J. Fluids Engng* **125**, 500–509.

- KRAJNOVIĆ, S. & DAVIDSON, L. 2005a Flow around a simplified car. Part 1. Large Eddy Simulation. *Trans. ASME J. Fluids Engng* **127**, 907–918.
- KRAJNOVIĆ, S. & DAVIDSON, L. 2005b Flow around a simplified car. Part 2. Understanding the flow. *Trans. ASME J. Fluids Engng* **127**, 919–928.
- KRAJNOVIĆ, S. & FERNANDES, J. 2011 Numerical simulation of the flow around a simplified vehicle model with active flow control. *Intl J. Heat Fluid Flow* **32** (5), 192–200.
- LAHAYE, A., LEROY, A. & KOURTA, A. 2014 Aerodynamic characterisation of a square back bluff body flow. *Intl J. Aerodyn.* **4** (1–2), 43–60.
- LIENHART, H. & BECKER, S. 2003 Flow and turbulent structure in the wake of a simplified car model. *SAE Paper No.* 2003-01-0656.
- LUMLEY, J. L. 1970 *Stochastic Tools in Turbulence*. Academic Press.
- MA, X. & KARNIADAKIS, G. E. 2002 A low-dimensional model for simulating three-dimensional cylinder flow. *J. Fluid Mech.* **458**, 181–190.
- NOACK, B. R., AFANASIEV, K., MORZYŃSKI, M., TADMOR, G. & THIELE, F. 2003 A hierarchy of low-dimensional models for the transient and post-transient cylinder wake. *J. Fluid Mech.* **497**, 335–363.
- NOACK, B. R. & ECKELMANN, H. 1994 A global stability analysis of the steady and periodic cylinder wake. *J. Fluid Mech.* **270**, 297–330.
- NOACK, B. R., MORZYŃSKI, M. & TADMOR, G. 2011 *Reduced-Order Modelling for Flow Control. (CISM Courses and Lectures)*, vol. 528. Springer.
- NOACK, B. R., PAPAS, P. & MONKEWITZ, P. A. 2005 The need for a pressure-term representation in empirical Galerkin models of incompressible shear flows. *J. Fluid Mech.* **523**, 339–365.
- NOACK, B. R., SCHLEGEL, M., AHLBORN, B., MUTSCHKE, G., MORZYŃSKI, M., COMTE, P. & TADMOR, G. 2008 A finite-time thermodynamics of unsteady fluid flows. *J. Non-Equilib. Thermodyn.* **33**, 103–148.
- ÖSTH, J. & KRAJNOVIĆ, S. 2012 The flow around a simplified tractor-trailer model studied by Large Eddy Simulation. *J. Wind Engng Ind. Aerodyn.* **102**, 36–47.
- ÖSTH, J. & KRAJNOVIĆ, S. 2014 A study of the aerodynamics of a generic container freight wagon using Large-Eddy Simulation. *J. Fluid. Struct.* **44**, 31–51.
- ÖSTH, J., KRAJNOVIĆ, S., BARROS, D., CORDIER, L., NOACK, B. R., BORÉE, J. & RUIZ, T. 2013 Active flow control for drag reduction of vehicles using Large Eddy Simulation, experimental investigations and reduced order modelling. *Proceedings of the 8th International Symposium on Turbulent and Shear Flow Phenomena (TSFP-8), Poitiers, France.*
- PASTOOR, M., HENNING, L., NOACK, B. R., KING, R. & TADMOR, G. 2008 Feedback shear layer control for bluff body drag reduction. *J. Fluid Mech.* **608**, 161–196.
- PODVIN, B. 2009 A proper-orthogonal-decomposition-based model for the wall layer of a turbulent channel flow. *Phys. Fluids* **21**, 015111 1..18.
- POPE, S. B. 2000 *Turbulent Flows*. 1st edn. Cambridge University Press.
- RAJAEI, M., KARLSSON, S. K. F. & SIROVICH, L. 1994 Low-dimensional description of free-shear-flow coherent structures and their dynamical behaviour. *J. Fluid Mech.* **258**, 1–29.
- REMPFER, D. & FASEL, F. H. 1994a Evolution of three-dimensional coherent structures in a flat-plate boundary-layer. *J. Fluid Mech.* **260**, 351–375.
- REMPFER, D. & FASEL, F. H. 1994b Dynamics of three-dimensional coherent structures in a flat-plate boundary-layer. *J. Fluid Mech.* **275**, 257–283.
- SCHLEGEL, M. & NOACK, B. R. 2013 On long-term boundedness of Galerkin models. *J. Fluid Mech.* (submitted).
- SCHLEGEL, M., NOACK, B. R., COMTE, P., KOLOMENSKIY, D., SCHNEIDER, K., FARGE, M., SCOUTEN, J., LUCHTENBURG, D. M. & TADMOR, G. 2009 Reduced-order modelling of turbulent jets for noise control. In *Numerical Simulation of Turbulent Flows and Noise Generation: Results of the DFG/CNRS Research Groups FOR 507 and FOR 508*, Notes on Numerical Fluid Mechanics and Multidisciplinary Design (NNFM), vol. 1, pp. 3–27. Springer.
- SIROVICH, L. 1987a Turbulence and the dynamics of coherent structures, part I: coherent structures. *Q. Appl. Math.* **45**, 561–571.

- SIROVICH, L. 1987*b* Turbulence and the dynamics of coherent structures, part II: symmetries and transformations. *Q. Appl. Math.* **45**, 573–582.
- SMAGORINSKY, J. 1963 General circulation experiments with the primitive equations. *Mon. Weath. Rev.* **91** (3), 99–165.
- SPOHN, A. & GILLIERON, P. 2002 Flow separations generated by a simplified geometry of an automotive vehicle. *IUTAM Symposium: Unsteady Separated Flows, Toulouse, France*.
- UKEILEY, L., CORDIER, L., MANCEAU, R., DELVILLE, J., BONNET, J. P. & GLAUSER, M. 2001 Examination of large-scale structures in a turbulent plane mixing layer. Part 2. Dynamical systems model. *J. Fluid Mech.* **441**, 61–108.
- VERZICCO, R., FATICA, M., LACCARINO, G. & MOIN, P. 2002 Large Eddy Simulation of a road vehicle with drag-reduction devices. *AIAA J.* **40**, 2447–2455.
- WANG, Z., AKHTAR, I., BORGGAARD, J. & ILIESCU, T. 2011 Two-level discretizations of nonlinear closure models for proper orthogonal decomposition. *J. Comput. Phys.* **230**, 126–146.
- WANG, Z., AKHTAR, I., BORGGAARD, J. & ILIESCU, T. 2012 Proper orthogonal decomposition closure models for turbulent flows: a numerical comparison. *Comput. Meth. Appl. Mech. Engng* **237–240**, 10–26.
- WASSEN, E. & THIELE, F. 2009 Road vehicle drag reduction by combined steady blowing and suction. *AIAA Paper* 2009-4174.